Toward a Global Map of Raindrop Size Distributions. Part I: Rain-Type Classification and Its Implications for Validating Global Rainfall Products

TRISTAN S. L'ECUYER, CHRISTIAN KUMMEROW, AND WESLEY BERG

Department of Atmospheric Science, Colorado State University, Fort Collins, Colorado

ABSTRACT

Variability in the global distribution of precipitation is recognized as a key element in assessing the impact of climate change for life on earth. The response of precipitation to climate forcings is, however, poorly understood because of discrepancies in the magnitude and sign of climatic trends in satellite-based rainfall estimates. Quantifying and ultimately removing these biases is critical for studying the response of the hydrologic cycle to climate change. In addition, estimates of random errors owing to variability in algorithm assumptions on local spatial and temporal scales are critical for establishing how strongly their products should be weighted in data assimilation or model validation applications and for assigning a level of confidence to climate trends diagnosed from the data.

This paper explores the potential for refining assumed drop size distributions (DSDs) in global radar rainfall algorithms by establishing a link between satellite observables and information gleaned from regional validation experiments where polarimetric radar, Doppler radar, and disdrometer measurements can be used to infer raindrop size distributions. By virtue of the limited information available in the satellite retrieval framework, the current method deviates from approaches adopted in the ground-based radar community that attempt to relate microphysical processes and resultant DSDs to local meteorological conditions. Instead, the technique exploits the fact that different microphysical pathways for rainfall production are likely to lead to differences in both the DSD of the resulting raindrops and the three-dimensional structure of associated radar reflectivity profiles. Objective rain-type classification based on the complete three-dimensional structure of observed reflectivity profiles is found to partially mitigate random and systematic errors in DSDs implied by differential reflectivity measurements. In particular, it is shown that vertical and horizontal reflectivity structure obtained from spaceborne radar can be used to reproduce significant differences in Z_{dr} between the easterly and westerly climate regimes observed in the Tropical Rainfall Measuring Mission Large-scale Biosphere–Atmosphere (TRMM-LBA) field experiment as well as the even larger differences between Amazonian rainfall and that observed in eastern Colorado. As such, the technique offers a potential methodology for placing locally observed DSD information into a global framework.

1. Introduction

In their most recent assessment, the Intergovernmental Panel on Climate Change (IPCC) identifies variability in the global distribution of precipitation as a key component in understanding the impact of climate change on the environment (McCarthy et al. 2001). As yet, however, the response of precipitation to climate forcings on annual and interannual time scales remains uncertain because of discrepancies in the magnitude and even the sign of rainfall variability on both global and regional scales in different satellite-based estimates such as the Global Precipitation Climatology Project (GPCP) (Huffman et al. 1997), Climate Prediction Center (CPC) Merged Analysis of Precipitation (CMAP) (Xie and Ar-

kin 1996, 1997), and Tropical Rainfall Measuring Mission (TRMM) Precipitation Radar (PR) (Iguchi et al. 2000) products. Recent studies suggest that these climate-regime-dependent biases originate from systematic changes in nonobservable parameters that must be assumed to solve the fundamentally underconstrained problem of retrieving rainfall from satellite observations (Berg et al. 2002). Regional and time-dependent variations in the vertical distribution of liquid and ice, the dielectric properties of mixed-phase hydrometeors, and the horizontal inhomogeneity of rainfall within the satellite field of view, for example, have all been identified as potential sources of systematic error in rainfall estimates from the TRMM Microwave Imager (TMI) (Nesbitt et al. 2000; Poyner 2002; Battaglia et al. 2003; Kummerow et al. 2004). Similarly, rainfall estimates from single-frequency radars without polarization capability, such as the TRMM PR, suffer from uncertainties associated with nonuniform beam filling and errors in assumed Z–R relationships because of temporal and

Corresponding author address: Tristan S. L'Ecuyer, Department of Atmospheric Science, Colorado State University, Fort Collins, CO 80523-1371.
E-mail: tristan@atmos.colostate.edu

spatial variations in raindrop drop size distributions (DSDs) (Iguchi et al. 2000; Amitai 2000; Zhang et al. 2001; Bringi and Chandrasekar 2001; Uijlenhoet et al. 2003). For example, Robertson et al. (2003) find that while interannual variability in path-integrated attenuation (PIA) from the PR closely matches the TMI rainfall time series, discrepancies exist between the observed PIA and the PR rainfall estimates themselves that are indicative of time-dependent biases in the assumed DSD. Quantifying and ultimately removing these uncertainties is critical for studying the response of the hydrologic cycle to climate change, validating model simulations of climate variability, and for data assimilation applications.

This paper seeks to address the problem of estimating and reducing systematic and random errors in satellite-based retrieval algorithms. Ultimately it is hoped that the technique outlined here will be applicable to a wide range of atmospheric remote sensing applications but, to fix ideas, we focus on the problem of retrieving rainfall globally from single-parameter (i.e., single-frequency and nonpolarimetric) radars, such as the TRMM PR. These algorithms seek to relate the fraction of an emitted pulse of radiation that is backscattered by a volume of the atmosphere to the amount of rainfall that falls from that volume. This problem is complicated by the fact that the backscattered fraction, known as the reflectivity, depends on both the concentration of raindrops within the volume and their size. Since it is impossible to simultaneously determine both properties from a single reflectivity measurement, it is necessary to specify raindrop size spectra prior to estimating rainfall, and these algorithms incur both random and systematic errors as a result.

The problems associated with applying climatological mean relationships between reflectivity and rainfall (known as Z–R relationships) are well understood by both the satellite and ground-based radar communities (e.g., Sempere-Torres et al. 2000; Lee 1990; Uijlenhoet et al. 2003). The ground-based radar community has approached this problem from the perspective of better understanding relationships between microphysical processes, raindrop DSDs, and the associated meteorological conditions in which they form (e.g., Sempere-Torres et al. 1999; Carey et al. 2001; Cifelli et al. 2002; Petersen et al. 2002; and Rickenbach et al. 2002). These studies make use of raindrop size distribution measurements from Joss and Waldvogel (1967), optical, and acoustic disdrometers, and/or multiparameter radars, fall speed observations from Doppler radars, and meteorological variables such as wind speed, aerosol content, etc. that can be used to identify the dominant microphysical processes at work and connect them to the properties of the climate regimes in which they occur.

Unfortunately, satellite-based algorithms do not have access to the detailed microphysical or regime information being used in ground-based studies. As such they have been forced to make general assumptions regarding DSD, which, in turn, cause algorithms to over- and underestimate regional rainfall. Furthermore, attempts to validate satellite rainfall estimates through comparisons between ground-based and satellite-based radars often demonstrate little more than the fact that locally derived DSDs differ from those assumed globally, providing limited insight into the accuracy of the latter on global scales. Regrettably, it is neither affordable nor practical to deploy disdrometers, rain gauges, or ground-based radars on the global scale to measure time–space mean DSDs or their variance. Since neither explicit microphysics nor DSD information can be gleaned from satellite observations alone, a different approach is required to identify microphysical processes and resulting DSDs using only radar reflectivity fields. The challenge facing global algorithm developers is, then, to develop a framework for importing information gleaned from local field experiments to constrain the global problem.

Because of its global nature, the approach developed here steers away from the observations related to the meteorological conditions and microphysical processes surrounding rainfall development. It seeks instead to relate DSD information obtained from ground observations to the vertical and horizontal structure of reflectivity measurements that can be observed from a spaceborne radar. The approach is based on the hypothesis that distinct microphysical processes give rise to distinguishable raindrop size distributions and, at the same time, manifest themselves as differences in the vertical and horizontal structure of observed radar reflectivity profiles. This idea is not completely new: reflectivity–rainfall relationships have been subjectively separated according to whether a pixel exhibited the characteristics of convective or stratiform rainfall for many years (see Battan 1973, and references therein). Rosenfeld et al. (1995) went a step further and used a set of parameters describing the three-dimensional structure of the reflectivity field to objectively classify rainfall observed at Darwin, Australia, into physically meaningful regimes. Recently, Boccippio (2003) used a cluster analysis to objectively classify rainfall on a global scale using PR data. We seek to adapt the concept outlined in these two papers to the problem of using observed radar reflectivity structure to objectively develop an ensemble of rainfall classes with the goal of assigning an appropriate set of DSD parameters to each using size distribution information from disdrometers or polarimetric radars where available. Since the relationship between a general set of microphysical processes and the resulting DSD is far from unique, we will further aim to determine the DSD variability within each rainfall class for later use as a measure of uncertainty.

To illustrate the general idea, consider the pathways for the formation of precipitation in two hypothetical air masses summarized in Fig. 1. The left-hand side applies to a cold-based cloud ($T < 0°$) perhaps residing in an aerosol-rich continental air mass while the right-hand side governs a warm-based cloud ($T > 0°$) in a
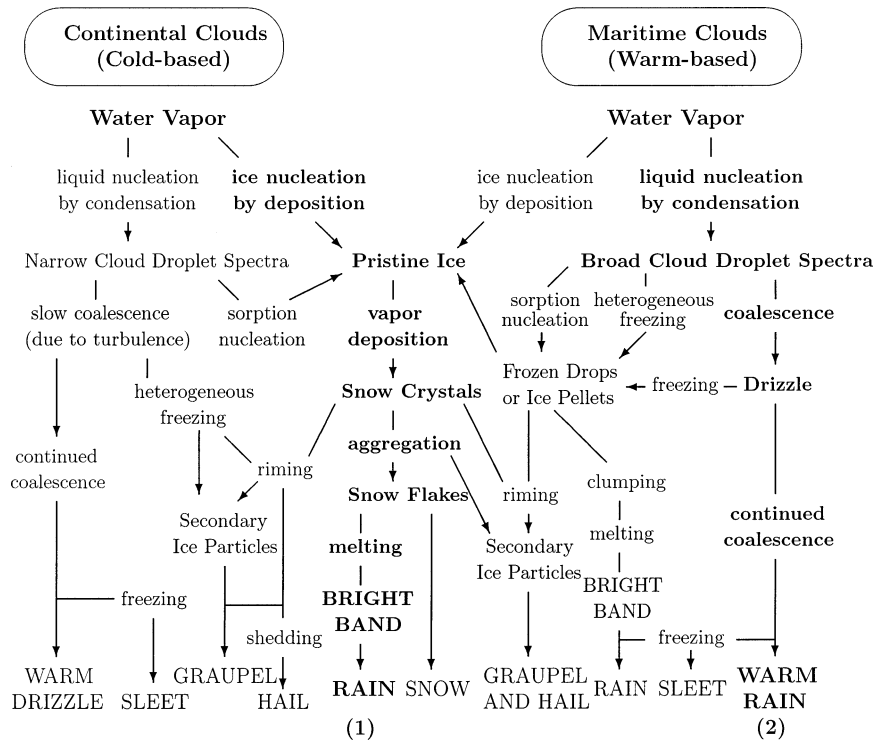
Continental Clouds (Cold-based) **Maritime Clouds (Warm-based)**

Water Vapor

liquid nucleation by condensation — **ice nucleation by deposition** ice nucleation by deposition — **liquid nucleation by condensation**

Narrow Cloud Droplet Spectra — **Pristine Ice** — **Broad Cloud Droplet Spectra**

slow coalescence (due to turbulence) — sorption nucleation — **vapor deposition** sorption nucleation — heterogeneous freezing — **coalescence**

heterogeneous freezing — **Snow Crystals** Frozen Drops or Ice Pellets ← freezing — Drizzle

continued coalescence — riming — **aggregation** riming — clumping — **continued coalescence**

Secondary Ice Particles — **Snow Flakes** Secondary Ice Particles — melting

freezing — shedding — **melting** BRIGHT BAND

BRIGHT BAND

WARM DRIZZLE — SLEET — GRAUPEL HAIL — **RAIN** — SNOW   GRAUPEL AND HAIL — RAIN — SLEET — **WARM RAIN**

freezing

(1) **(2)**

FIG. 1. Selected pathways for precipitation formation from (left) cold-based continental clouds and (right) warm-based maritime clouds (adapted from Cotton and Anthes 1989). Two distinct pathways discussed in the text are labeled (1) and (2) and highlighted in bold.

cleaner air mass. For the purposes of illustration, two distinct pathways leading to liquid precipitation have been highlighted in bold. The first corresponds to development of precipitation through cold cloud processes starting with an initial distribution of ice crystals that grow through riming and aggregation into snowflakes and ultimately melt at warmer temperatures near the surface, giving rise to liquid precipitation. The reflectivity profile resulting from this type of rain event is characterized by relatively low but finite reflectivities from large ice particles at upper levels, a layer of intense reflectivity from large melting snow flakes near the melting level [known as the radar bright band (BB)], and moderate reflectivities below the BB. The slope of the reflectivity profile below the BB is determined by the relative humidity at lower levels of the atmosphere. Provided lower levels are at or near saturation with respect to liquid, the reflectivity profile will be uniform in height down to the surface. Subsaturation, on the other hand, results in evaporation at lower levels and a substantial decrease in reflectivity with decreasing altitude. Rainfall emerging at the surface from this pathway is characterized by larger than average raindrops relative to other pathways. Furthermore, since smaller drops evaporate more readily than larger ones, rainfall that falls through a subsaturated environment at lower levels will, on average, exhibit still larger droplets.

Through the second pathway, precipitation develops in the absence of any ice-phase microphysical processes. In a saturated environment, liquid cloud droplets form through condensation onto relatively few aerosol particles. The absence of additional nuclei allows a number of these droplets to grow to larger sizes, resulting in a broad spectrum of cloud droplet sizes required for vigorous collision and coalescence to occur. Drizzle soon forms as a result, and continued coalescence eventually leads to liquid precipitation. Since this precipitation, commonly referred to as "warm rain," develops entirely at temperatures at or above freezing, it results in a shallow reflectivity profile. Further, the lack of large melting ice particles at the melting level suppresses the radar BB common in many mixed-phase precipitation events. By similar arguments, the fact that precipitation forms exclusively through collision and coalescence of liquid cloud droplets results in smaller raindrops, on average, than those resulting from the melting of large snow-flakes. Observations from a ground-based radar in a region characterized by both types of precipitation may be able to explicitly distinguish these two pathways based on ancillary information regarding the large-scale conditions in the area provided a focused field experiment had, at some time, been conducted to explore the origins of each in terms of the properties of the local environment. However, since the relationships between DSD and local meteorology vary greatly from place to place and over time, focused field experiments cannot

be used to constrain DSDs in global algorithms, requiring a new approach to the problem. Fortunately, in both examples there appears to be a connection between the structure of the expected reflectivity profile and the size distribution of the resulting raindrops.

While complicated in its own right, Fig. 1 represents only a limited number of idealized microphysical processes governing the exchange of water between vapor, liquid, and ice phases. The cycling of water between these reservoirs in the earth's atmosphere is, in reality, extremely sensitive to the thermodynamic, chemical, and dynamical properties of the surrounding environment, leading to a myriad of complex pathways for precipitation development. Even so, the simplified examples presented above suggest that distinct combinations of microphysical processes will give rise to different vertical and horizontal radar reflectivity profiles, which we postulate should provide a means of constraining DSDs. It is our contention that while rain systems vary greatly from region to region and in time, the fundamental connection between reflectivity structure and DSD established by the microphysical mechanisms underlying rainfall development is more or less universal. Thus reflectivity structures may provide a link between satellite observables and variables measured by ground-based polarimetric radars that will allow DSD parameters consistent with the local environment to be assigned to single-frequency reflectivity profiles.

To test this hypothesis, polarimetric radar observations from the joint TRMM Large-scale Biosphere Atmosphere (LBA) field experiment in Rondonia, Brazil, and the Colorado State University–University of Chicago and University of Illinois, Champaign (CSU–CHILL) radar facility in northeastern Colorado are examined to assess the extent to which similar rainfall structures, or rain-type classes,[1] found in both regions exhibit more or less universal DSD properties. It is our goal to explore the potential for projecting DSD information obtained from ground-based observations onto the reflectivity structure observed by the TRMM PR. Furthermore, if care is taken to construct rainfall retrieval algorithms with complete end-to-end error models, we expect that the variability of DSD parameters within any given rain-type class and systematic differences in these parameters arising from climate regime

---

[1] Before proceeding a brief explanation is needed regarding the desired interpretation of the term ''rain type'' in the context of this study. In many applications it is natural to assign a physical interpretation to each rain type, perhaps in terms of the specific microphysical processes, kinematic properties, or thermodynamic characteristics governing its occurrence. The goals of this study are, however, rooted in the realm of algorithm development and validation and, as a result, warrant a more mechanical definition of each rain type based entirely on the measurements used to define it. It will be shown that thousands of rain types must be introduced in order to make statistically significant progress toward describing DSD, and, while some microphysics-based interpretation will be offered for differences between some example rain types, it is impractical to seek unique descriptions for all that are defined.

dependencies can be translated into an uncertainty in retrieved rainfall rate.

2. Identifying rain types

Conventional approaches to rain-type classification are generally based on a subjective separation of rainfall into two types: 1) convective precipitation characterized by strong updrafts, significant horizontal variability, and little or no evidence of a BB, and 2) stratiform precipitation characterized by horizontally homogeneous rainfall in regions of weak and uniform ascent and a well-defined BB at the freezing level. This has been the prevailing approach for nearly half a century and is particularly useful for estimating latent heating in precipitating systems since, to first order, stratiform and convective rainfall exhibit distinct vertical distributions of latent heating. The DSD, critical for quantitative radar-based rainfall retrievals, however, varies widely within the convective and stratiform categories requiring additional information to further constrain such algorithms. In this paper we explore the possibility of extending rain-type classification beyond traditional convective/stratiform separation to objectively define a set of rain types that constrain DSD and provide a framework for determining its mean and variability from auxiliary ground validation data. This involves determining the set of observables that provide the most information regarding DSD and the resolution to which they must be binned to define rain types that optimally constrain DSD parameters in a retrieval algorithm. Rather than approaching the problem with the hope of presenting the final word on either of these considerations, the goal of this section is to develop a procedure for assessing the best set of classification variables from an arbitrary list and to provide a set of criteria for establishing the binning resolution needed for using them in a rain-type classification scheme.

a. Data and choice of variables

Eleven variables are chosen that are related to the vertical and horizontal structure of an observed reflectivity field: surface reflectivity, vertical gradients between 0.5 and 2 km, 2 and 4 km, 4 and 6 km, and 6 and 8 km, the height of the maximum reflectivity, its ratio to that at the surface, the ratio of the integrated reflectivity above the freezing level to that at the surface, the highest altitude with a radar echo above 20 dBZ, and the mean and maximum of the horizontal gradient in surface reflectivity between each pixel and its eight nearest neighbors. These variables are chosen because they represent a number of elements related to the microphysical processes depicted in Fig. 1, notably, the intensity of rainfall at the surface, the amount of evaporation at lower levels, the ice content aloft, and the strength of the bright band. Since it is important to keep the number of variables and resulting classes as low as

possible to maintain conceptual simplicity and to provide a tractable algorithm from a computational standpoint, the first step in defining the classification grid is to isolate the subset of variables that carry independent information. To this end, correlations between all variables are examined using S-band (10.7 cm) polarimetric radar data collected using the National Center for Atmospheric Research (NCAR) S-band Dual Polarization Doppler Radar (S-Pol) that was deployed during the TRMM-LBA field experiment that took place in the Amazon wet season from 10 January to 28 February 1999. (For a detailed overview of the TRMM-LBA experiment, the reader is referred to the CSU TRMM-LBA Web site at http://olympic.atmos.colostate.edu/lba.trmm.) S-Pol collected observations of reflectivity, differential reflectivity, linear depolarization ratio, and total differential phase, all of which have been processed to remove the effects of ground clutter, anomalous propagation, second-trip echoes, partial beam blocking, attenuation by precipitation, calibration biases, and clear-air echoes. Details regarding the processing methodology and validation of this dataset can be found in Carey et al. (2000). Initially the datasets produced by Carey et al. (2000) are gridded to 2-km horizontal and 0.5-km vertical resolution assuming a 1-km radius of influence for the interpolation in each direction. These data have subsequently been gridded to 4-km resolution in the horizontal to be consistent with the spatial resolution of the TRMM PR. This also alleviates the more practical issue that the quality of the vertical profiles inferred from radar volume scans decreases with range from the radar because of the decrease in density of observations and increasing sample volume with increasing range (Zawadzki and Bellon 2003). For the same reason, the analysis focuses on data within a range of 100 km from the radar. The resulting dataset consists of 6074 scans taken approximately every 10 min during the experiment, providing more than 365 000 raining pixels with suitable data with which to develop the classification.

Finally, the data have been subsetted into the easterly and westerly meteorological regimes identified by Rickenbach et al. (2002) based on observations of the large-scale dynamics in the region (see also Carey et al. 2001 and Petersen et al. 2002). The easterly regime is characterized by significantly larger CAPE, drier lower-and middle-tropospheric humidity, a stronger and deeper wind sheer layer, and a factor of 2 higher concentration of cloud condensation nuclei (CCN) than in the westerly regime (Williams et al. 2002). Carey et al. (2001) further note that raindrops in the westerly regime are generally smaller than those found in the easterly regime for a given reflectivity bin. This provides an important test for the rain-type classification system. While local radar operators can generally identify the prevailing climate regime using the wind direction, satellites cannot rely on such knowledge on global scales. As a result, the classification approach must be capable of detecting this DSD difference independent of ancillary data.

Analysis of the correlations between variables computed from the complete LBA dataset indicates that the height of the maximum observed reflectivity signal, the integrated reflectivity above the freezing level, and the maximum horizontal gradient are all sufficiently highly correlated with other variables as to make them redundant from the classification standpoint. These variables are therefore eliminated, leaving the eight illustrated in Fig. 2 to be used in developing the classification. It is worth noting that a more rigorous empirical orthogonal function (EOF) analysis indicated that more than 95% of the variance in the LBA dataset could be explained by the first six EOFs. In an operational implementation of the algorithm, this property may be used to reduce the dimensionality of the classification grid, potentially reducing computation time. This is, however, left as an exercise for the future, and the original variables are preserved for the present study to facilitate interpretation of the results.

Since the primary objective of rain-type classification in this paper is to reduce variability in DSD, the variability in differential reflectivity, Z_{dr}, in each rain-type class is adopted to assess its performance relative to the unclassified dataset. In rainfall, the differential reflectivity, defined as the ratio of the scattering intensities at horizontal and vertical polarization,

$$Z_{dr} = 10 \log_{10} \frac{|S_{HH}|^2}{|S_{VV}|^2}, \qquad (1)$$

provides a measure of the reflectivity-weighted axis ratio of the raindrops in the sample volume (Jameson 1983). As a result, Z_{dr} is related to DSD since a raindrop becomes increasingly oblate the larger it gets, owing to hydrodynamic forces. The numerical model for the axis ratio, $r = b/a$, of a raindrop proposed by Beard and Chuang (1987), for example, can be reasonably approximated by

$$r = a + bD + cD^2 + dD^3 + eD^4, \qquad (2)$$

where $a = 1.0048$, $b = 5.7 \times 10^{-4}$, $c = -2.628 \times 10^{-2}$, $d = 3.682 \times 10^{-3}$, and $e = -1.677 \times 10^{-4}$ for raindrops with diameters, D, between 0.5 and 7 mm. The larger the droplet, the more oblate it becomes and the larger the observed Z_{dr}. So, in principle, one can infer drop size from Z_{dr}. Bringi and Chandrasekar (2001), for example, couple the Beard and Chuang (1987) axis ratio parameterization with an assumed gamma DSD to arrive at a fit for the mass-weighted mean drop diameter of the form $D_m = 1.619 Z_{dr}^{0.485}$.

It is important to note that there are a variety of uncertainties associated with inverting Z_{dr} observations to obtain drop size. First, for a polydispersed DSD, Z_{dr} is biased toward the largest drops since reflectivity is proportional to drop diameter to the sixth power in the Rayleigh–Gans limit. Thus Z_{dr} based retrievals of drop size are particularly sensitive to the assumed shape of the DSD since they depend strongly on the large particle tail of the distribution. Furthermore, canting and drop
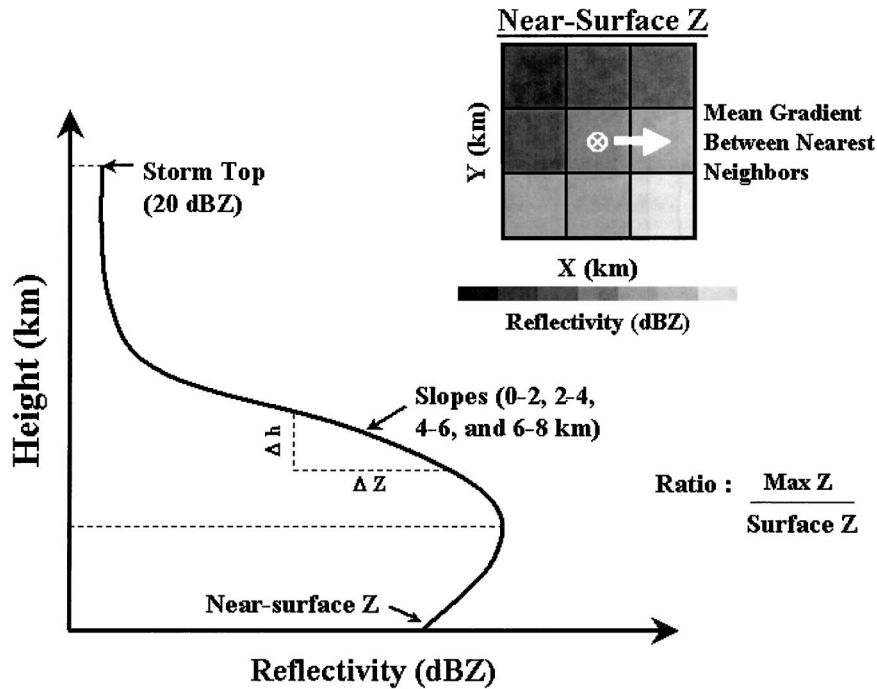
FIG. 2. Variables describing the three-dimensional structure of an observed reflectivity field used for classifying rainfall.

oscillations can lead to uncertainties in relating the measured Z_{dr} to axis ratio (Bringi and Chandrasekar 2001). To avoid these issues influencing the results, the remainder of the analysis in the present paper is conducted in Z_{dr} space with the understanding that the results should, in principle, apply to DSD itself. Even in Z_{dr} space, however, the analysis is susceptible to random and systematic errors in the Z_{dr} measurements themselves. The bias in the Z_{dr} estimates employed in the present study is expected to be on the order of 0.1 dB (Carey et al. 2000), while random noise is likely ∼0.1–0.3 dB. As a result, some random variability in Z_{dr} is likely to remain even if the data were perfectly classified. This random noise should, however, be significantly reduced when many pixels are averaged together, a fact that provides the motivation for restricting the subsequent analyses to classes that are sampled at least 20 times.

If Z_{dr} is considered a proxy for drop size, then it is logical to seek a bin size for the eight remaining variables that provides the greatest reduction in its variability, $\sigma_{Z_{dr}}$, over all pixels that fall into each rain type. In addition, it is desirable to minimize differences in the mean Z_{dr} within any given rain type when it is observed in distinct climate regimes (e.g., different locations on the globe or during different seasons at the same location). Finally, it is desirable to represent as much rainfall as possible with as few rain types as possible.

b. The method of untrained classification

To keep the analysis objectively based, the dataset is processed using the technique of untrained classification. The first pixel in the dataset is designated as the first rain-type class. The vertical and horizontal structure of the second pixel is then compared with the properties of the first and is considered to belong to the same rain-type class if the root-mean-square (rms) difference between its structure properties and those of the first is less than some prescribed threshold, that is,

$$\sqrt{\frac{\sum_{i=1}^{M} (x_i^{\text{pixel}} - x_i^{\text{class}})^2}{M^2}} \le \chi, \qquad (3)$$

where the x_i represent standardized[2] vertical and horizontal structure variables, and χ denotes the chosen threshold. If Eq. (3) is not satisfied, it defines a new rain-type class. The process is then repeated for all subsequent pixels in the dataset. Each is compared, in turn, with the properties of all rain-type classes defined before it. If Eq. (3) is satisfied for a particular class, the pixel is assigned to it and the processing moves on to the next pixel. Any pixel that fails to fall into any of the previously established classes defines a new one. To

[2] A variable is standardized by subtracting its mean and dividing by its standard deviation over the LBA dataset, $x_i = (y_2 - \overline{y_2})/\sigma_2$. If this is not done, differences in units result in some variables being weighted more than others in the rms difference.

OCTOBER 2004

L'ECUYER ET AL.

837

Original Westerly Regime Pixels
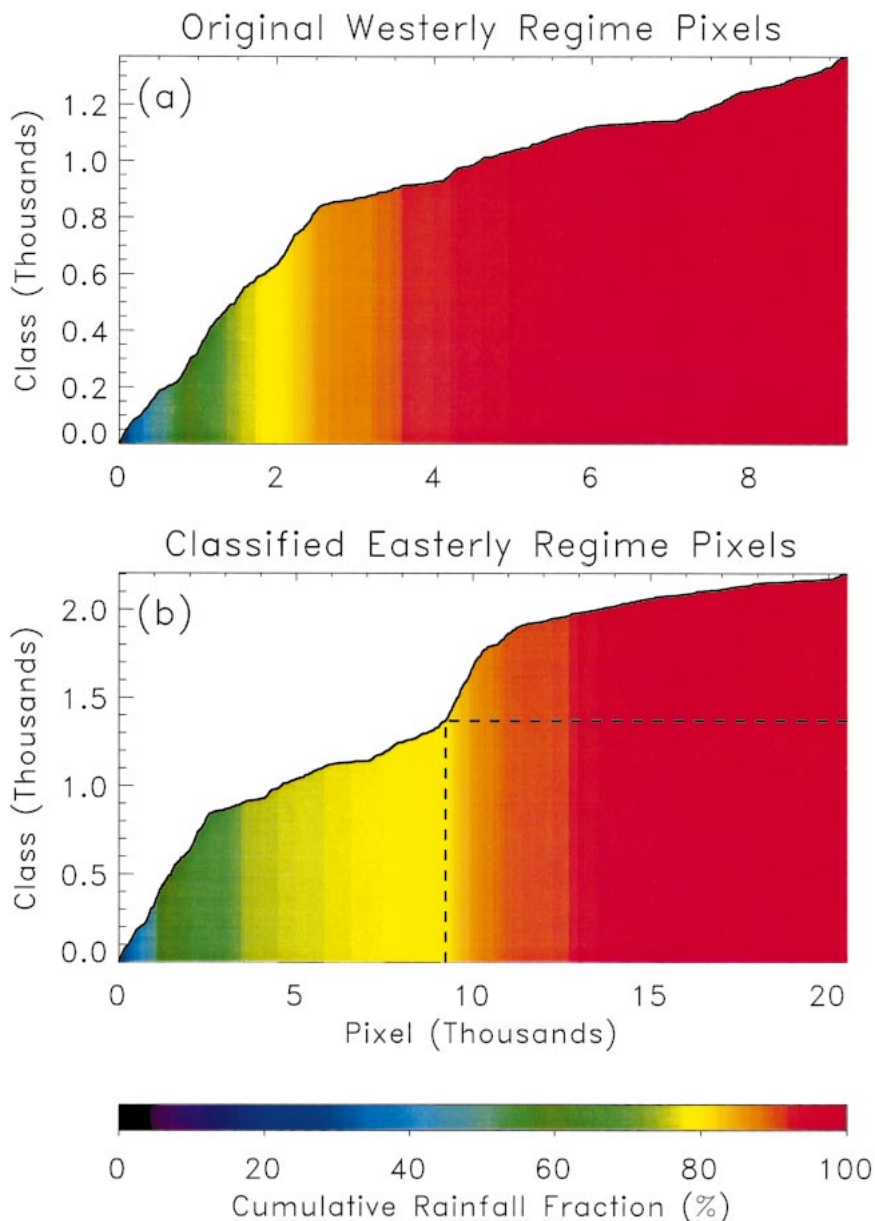

Classified Easterly Regime Pixels

FIG. 3. (a) Number of classes defined and fraction of rainfall classified through unsupervised classification of all westerly regime pixels with near-surface reflectivity of 36 ± 2 dBZ and at a threshold of 0.4. (b) As in (a), but for easterly regime pixels classified in terms of predefined classes from the westerly regime.

avoid manipulating enormous datasets that incur prohibitively long computation times, the data are first stratified by Z_{sfc} into four dBZ bins since drop size generally increases with increasing reflectivity. All profiles within each of these subsets are then sorted into classes according to the remaining seven classification variables using Eq. (3).

Figure 3a presents the number of rain types defined as a function of the number of pixels searched in the classification of all westerly regime pixels with near-surface reflectivities, Z_{sfc}, between 34 and 38 dBZ at a

threshold of $\chi = 0.4$. The shading beneath the curve represents the fraction of this rainfall subset that is explained by rain types in the classes defined up to that point. In this case, ~1350 distinct rain types are identified from the 9000 pixels examined, but more than 80% of the rainfall in the dataset can be attributed to the rain types defined over the first quarter of the pixels or, equivalently, the first 600 classes. While new rainfall events invariably identify new rain types, a majority of the reflectivity structures observed in the last three-quarters of the dataset are defined by prior rain events. This
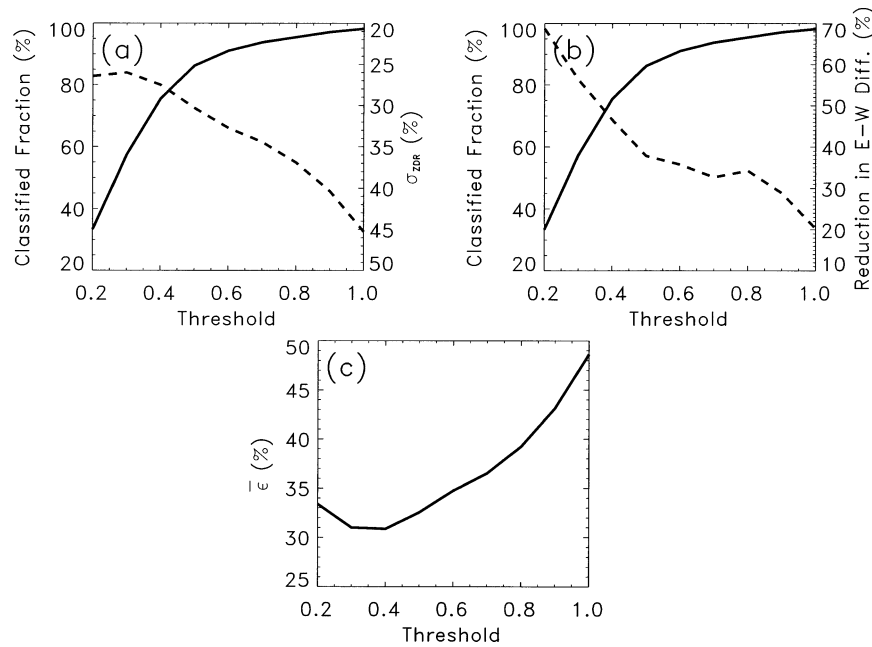
FIG. 4. (a) Trade-offs between the fraction of rainfall classified [solid line in (a) and (b)] and the random error in Z_{dr} and (b) reduction in systematic bias between easterly and westerly climate regimes. (c) Resulting uncertainty in assigned Z_{dr} from Eq. (5). Results apply to all pixels in the LBA dataset with near-surface reflectivity of 36 ± 2 dBZ.

fact is reinforced by Fig. 3b, which presents the classification of all easterly regime pixels with Z_{sfc} between 34 and 38 dBZ in terms of the rain types defined by the westerly regime. All pixels to the left of the vertical dashed line correspond to easterly regime pixels that were assigned rain types defined in the westerly regime. Despite the known differences in the character of the precipitation between the two regimes, less than 25% of the total rainfall in the easterly subset defines new rain types, and fewer than 850 new classes are defined from the more than 12 500 pixels examined.

c. Estimating an optimal threshold

Untrained classification as defined above provides a useful tool for objectively grouping pixels with similar properties, but the results depend critically on the apparently arbitrary choice of the threshold, χ. It can be argued, for example, that the case shown in Fig. 3 defines an unreasonably large number of rain types, and it is difficult to defined the choice of $\chi = 0.4$ in the absence of additional information. Returning to the LBA dataset, however, and recalling the purpose of developing the rain-type classification in the first place, an optimal threshold can be determined. It is reasonable to require that the optimal threshold be that which simultaneously maximizes the amount of rainfall falling into each class and minimizes the variability of Z_{dr} within any given class. More importantly, since the classification is designed to constrain DSD in global algorithms, a threshold must be chosen that minimizes the

differences in the mean Z_{dr} of classes that are found in both the easterly and westerly regimes. The solid curve in Figs. 4a and 4b indicates the fraction of easterly regime rainfall that is assigned to rain types defined using westerly regime data as a function of threshold, χ. Only pixels with surface reflectivities in the range 34–38 dBZ are presented in the figure, but similar results are obtained for other reflectivity ranges. The lower the threshold the more strictly a pixel's reflectivity structure has to match that of the class to which it is being compared. As a result, the fraction of easterly regime rainfall that fits into westerly rain types increases with increasing threshold. The dashed curve in Fig. 4a presents the standard deviation of Z_{dr} for all pixels in each class averaged over all classes in the reflectivity range. In Fig. 4b it represents the average reduction in the Z_{dr} difference between all classes found in both the regimes, defined as

$$\Delta_{\delta Z_{dr}} = 100 * \frac{|(\overline{Z_{dr,E}} - \overline{Z_{dr,W}})_{all} - (\overline{Z_{dr,E}} - \overline{Z_{dr,W}})_{class}|}{|(\overline{Z_{dr,E}} - \overline{Z_{dr,Wall}})|},$$

(4)

where the subscripts E and W denote easterly and westerly regimes, respectively. The subscript *all* refers to the mean properties of these regimes before classification, while the subscript *class* corresponds to an individual class found in the corresponding regime. A value of $\Delta_{\delta Z_{dr}} = 0$ corresponds to the limit where classification provides no information to reduce the Z_{dr} bias between regimes, while a value of 100 indicates that all of the

TABLE 1. Description of the final classification grid. The maxima and minima are representative of S-Pol data from TRMM-LBA but may need to be modified when applied to an alternate dataset.

Variable	Min	Max	Bin size	No. of bins
Z_{sfc} (dBZ)	4.0	56.0	4.0	13
Slope 0–2 km (dBZ km^{-1})	−8.0	8.0	1.0	16
Slope 2–4 km (dBZ km^{-1})	−7.0	9.0	2.0	8
Slope 4–6 km (dBZ km^{-1})	−15.0	5.0	2.5	8
Slope 6–8 km (dBZ km^{-1})	−15.0	6.0	3.0	7
Z_{max}/Z_{sfc} (dBZ/dBZ)	1.0	1.5	0.1	5
20 dBZ height (km)	2.0	14.0	1.5	8
Mean horizontal gradient (dBZ km^{-1})	0.0	6.0	1.0	6

bias is removed by classification. Clearly, rain types defined at tighter thresholds result in better constraints on Z_{dr} both through the reduction of its variability within any given class and improved uniformity of its mean value between the different climate regimes.

Now, returning to the global rainfall retrieval problem, all observed pixels that fall into a class whose properties have been defined through ground-based observations should be assigned a Z–R relationship based on the mean Z_{dr} or, equivalently, the mean DSD, for that class with the appropriate reduced uncertainty. All others can, at best, be assigned a mean Z–R relationship derived from the dataset as a whole with the associated large uncertainty; in other words, the algorithm must resort back to the climatological mean Z–R relationship. Now suppose the easterly regime pixels represent a set of satellite observations to be classified and assigned properties based on the westerly regime data. For any given threshold, a rough estimate of the average uncertainty in Z_{dr} assigned to all easterly regime rainfall is

$$\overline{\epsilon} = f\sigma_{Z_{dr}} + (1 - f)\sigma_{easterly}, \qquad (5)$$

where f is the fraction of easterly regime rainfall that falls into westerly regime rain types, $\sigma_{Z_{dr}}$ is the mean standard deviation in Z_{dr} for all classified easterly pixels, and $\sigma_{easterly}$ is the standard deviation in Z_{dr} over all pixels in the easterly regime. Figure 4c presents $\overline{\epsilon}$ as a function of threshold for all easterly pixels with surface reflectivities in the range 34–38 dBZ. The minimum of this curve corresponds to the lowest possible average uncertainty in easterly regime pixels when classified according to the rain types identified in the westerly regime dataset. This confirms that 0.4 is the optimal threshold for rain-type classification based on the eight variables described above. Analysis of other surface reflectivity ranges yields similar results, indicating that the optimum threshold should lie between 0.25 and 0.5.

It is impractical to perform the full untrained classification procedure on every new pixel the satellite encounters, as it requires comparison to thousands of existing classes. Instead, the optimal threshold is used to determine an appropriate set of equally spaced bins in the eight classification variables. Assuming a threshold of 0.4, the standard deviation of each of the eight classification variables averaged over all rain-type classes

defines the dimensions of an evenly spaced eight-dimensional grid onto which satellite observations can be mapped. In other words, the binning resolution in the *jth* variable is given by

$$\Delta_j = \frac{\sum_{i=1}^{N} (\sigma_{X_j})_i}{N}, \qquad (6)$$

where σ_{X_j} is the standard deviation of the variable X_j over all pixels assigned to a particular class, and *i* runs over all rain-type classes identified in the dataset. Table 1 provides the ranges and resolutions for each variable in defining the final classification grid. These dimensions result in more than 22 million possible rain-type classes, but it is important to note that many of these classes constitute unphysical combinations of variables that are never likely to be observed. Fewer classes restricts our ability to constrain the variability of polarimetric parameters within each rain type, while more classes reduces the number of times each raintype is sampled in validation experiments, resulting in poor statistics with which to determine appropriate mean polarimetric parameters and their standard deviations.

3. Properties of rain-type classes

a. Easterly and westerly climate regimes in TRMM-LBA

To test the hypothesis that rain-type classification may provide a useful tool to constrain DSD in satellite-based retrieval algorithms, it is important to determine the extent to which it can distinguish distinct climate regimes in a dataset. By virtue of its two meteorological regimes and the known differences in DSD they produce, the TRMM-LBA dataset is a particularly good example of a case in which systematic biases in rainfall estimates would be incurred if a climatological mean Z–R relationship were applied uniformly across the dataset. Figure 5 illustrates the variability in Z_{dr} for various subsets of the TRMM-LBA dataset, each based on using different information to classify the data. For purposes of illustration, only pixels with near-surface reflectivities in the range 36–40 dBZ are presented. Figure 5a represents the scenario in which no rain-type classification is used, allowing the full range of DSD variability
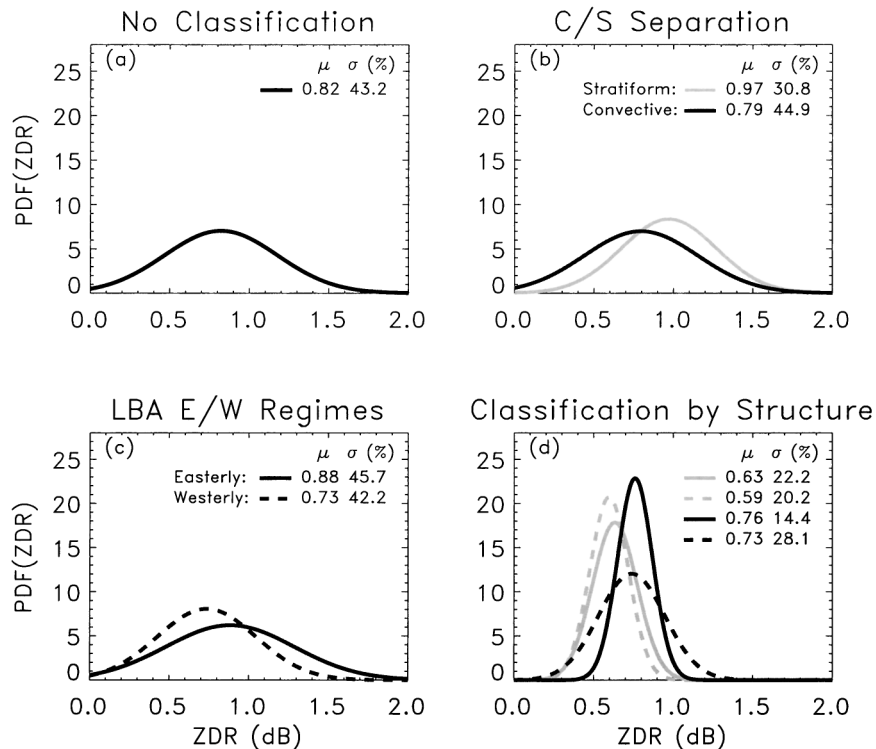
FIG. 5. Different methods for classifying the rainfall observed in the TRMM-LBA field experiment. Distributions of differential reflectivity Z_{dr} for (a) all raining pixels viewed by S-Pol (12 105 samples), (b) all raining pixels viewed by S-Pol but separated into convective and stratiform rainfall (11 831 and 274 samples, respectively), (c) all pixels determined to be convective in (b) further separated into easterly and westerly regimes as defined by Rickenbach et al. (2002) (5319 and 644 samples, respectively), and (d) two convective rainfall classes (represented by light and dark curves) observed in both the easterly (solid) and westerly (dashed) regimes in TRMM-LBA (>20 samples each). In all cases, statistics are restricted to profiles with near-surface reflectivities of 38 ± 2 dBZ.

indicated by the broad probability density function (PDF) of Z_{dr}.

Most current algorithms adopt a reflectivity-based classification into convective and stratiform rainfall categories that account for the fundamental differences in their microphysical, thermodynamic, and kinematic properties. The Steiner et al. (1995) technique, for example, examines the intensity and spatial uniformity of the low-level reflectivity field to identify convective (high intensity, nonuniform) and stratiform (low intensity, uniform) regions. This approach has been adapted and applied to the TRMM-LBA dataset by Carey et al. (2000), and the resulting PDFs of Z_{dr} for convective and stratiform pixels are illustrated in Fig. 5b. Clearly, this partitioning identifies the fact that, for a given rainfall intensity, convective raindrops are, on average, smaller than those found in stratiform rainfall, thereby reducing biases introduced by using a uniform Z–R relationship for all pixels. As Fig. 5b shows, however, the variability of DSDs within the convective and stratiform rain types is almost as large as with no classification at all, leading to large uncertainties in retrieved rainfall rates.

Perhaps more importantly, this wide range of DSDs

opens the door to systematic errors due to climate regime biases as can be seen in Fig. 5c, where the convective rainfall is further separated into the easterly and westerly wind regimes observed in TRMM-LBA. This case demonstrates the distinction between the ground-based and satellite-based approaches to constraining DSD in radar rainfall algorithms. Based on numerous ancillary datasets collected during the field campaign, Carey et al. (2001), Rickenbach et al. (2002), Cifelli et al. (2002), and others have determined that mean drop sizes in the easterly regime are larger than those found in the westerly regime and have related this finding to differences in the meteorological conditions and microphysical processes at work during each regime. If Z–R relationships failed to account for these differences, easterly rainfall will be overestimated and westerly rainfall underestimated. Given the available ancillary observations (most notably large-scale wind direction) local radar algorithms can, in principle, adopt a Z–R relationship appropriate to each regime. By virtue of their global coverage, however, satellite-based radar algorithms rarely encounter a region where the properties of local climate regimes have been studied to the extent
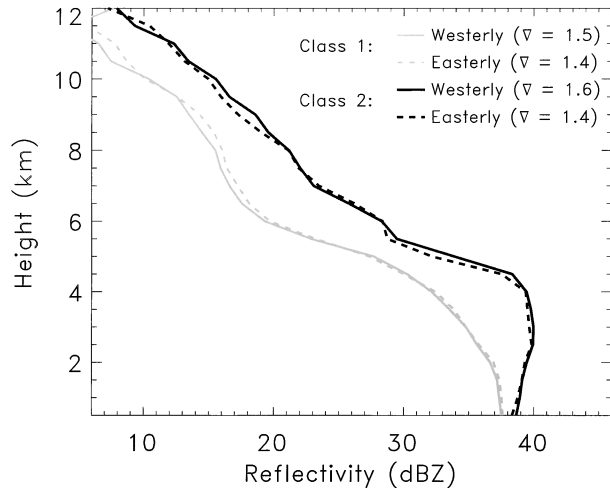
FIG. 6. Mean vertical profiles of radar reflectivity for the two classes highlighted in Fig. 5d in both the easterly and westerly regimes of LBA. Mean horizontal gradients between nearest neighbors are provided in parentheses in the legend.
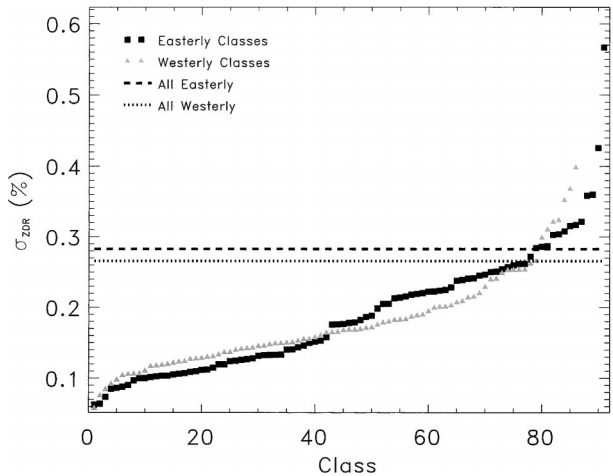

FIG. 7. Standard deviation of Z_{dr} for all classes with near-surface reflectivity of 38 dBZ (± 2) in the easterly (squares) and westerly (triangles) regimes of LBA. The dashed and dotted lines correspond to the entire easterly and westerly regimes, respectively.

of those found in TRMM-LBA. As a result, ancillary meteorological data do not provide sufficient information with which to constrain DSD in global algorithms, and they must rely on a satellite-observable-based form of classification such as that described above. The true test of such an approach is to assess whether or not it can constrain DSD regardless of climate regime. The analysis in section 2 ensures that the classification reduces easterly–westerly Z_{dr} differences in the mean sense, but it is instructive to look at a few specific examples. PDFs of Z_{dr} for two classes from the rain-type classification developed above that are found in both the easterly and westerly regimes are presented in Fig. 5d. Mean Z_{dr}'s observed in each class differ widely from one another, but pixel classification by reflectivity structure is found to capture these differences in both regimes. Furthermore, random errors due to variability within the classes are ~75% lower than those in any of the three preceding classification systems.

The correlation between reflectivity structure and DSD is evident when Fig. 5d is compared with the mean reflectivity profile for each class presented in Fig. 6. Note how the strong similarity between reflectivity profiles from the easterly and westerly regimes for the same rain type translates into a reduction in the Z_{dr} bias between the two regimes. Both the PDFs of Z_{dr} and the reflectivity structure can be connected to microphysical processes governing rainfall formation in each case. The reflectivity profiles indicate that class 2 exhibits more pronounced increase in reflectivity with height between the surface and 3 km, a thicker liquid water column perhaps indicative of the presence of supercooled droplets lofted above the freezing level and much larger reflectivities aloft. These characteristics suggest more vigorous mixed-phase microphysics and more evapo-

ration at lower levels, both of which produce larger raindrops and, hence, larger Z_{dr}, than class 1.

Looking beyond these specific examples to the dataset as a whole, Figs. 7 and 8 evaluate the overall performance of rain-type classification in reducing random and systematic errors in Z_{dr}, respectively. The standard deviations in Z_{dr} for all rain-type classes having near-surface reflectivities between 36 and 40 dBZ are presented in Fig. 7. This reflectivity range is highlighted for two reasons: 1) it spans the range of reflectivities for which Z_{dr} differences between the easterly and westerly regimes are the largest (Carey et al. 2001), providing the most challenging test of the classification ap-
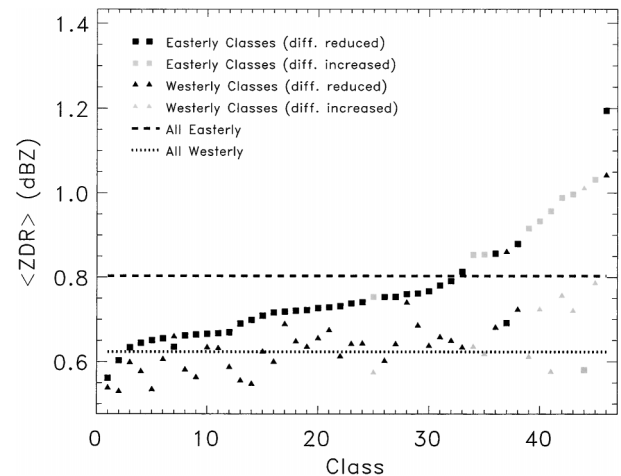

FIG. 8. Mean Z_{dr} for all mutual classes with near-surface reflectivity of 38 dBZ (± 2) in the easterly (squares) and westerly (triangles) regimes in LBA. The dashed and dotted lines correspond to the entire easterly and westerly regimes, respectively. Dark data points correspond to cases where the difference is reduced relative to the unclassified regimes, while light points represent classes for which the difference increases.

TABLE 2. Classification performance with respect to reducing $\sigma_{Z_{dr}}$ within the easterly and westerly regimes of TRMM-LBA for various surface reflectivity bins. The second and fifth columns indicate the total number of classes with at least 20 samples in each regime. The fraction of easterly and westerly regime rainfall these classes represent is summarized in the third and sixth columns, respectively. Finally, the fraction of this rainfall for which $\sigma_{Z_{dr}}$ is reduced in each regime is presented in the fourth and last columns.

Reflectivity range	N_E	$f_{E,\text{rain}}$	$f_{E,\text{reduced}}$	N_W	$f_{W,\text{rain}}$	$f_{W,\text{reduced}}$
28–32	232	63%	92%	253	66%	95%
32–36	183	62%	84%	171	56%	93%
36–40	91	43%	85%	86	41%	94%
40–44	45	34%	95%	33	27%	100%

proach, and 2) it is representative of a large fraction of the total rainfall in the dataset. To focus on statistically significant results and to reduce noise in the Z_{dr} measurements, only classes that are observed at least 20 times in either the easterly or westerly wind regimes are presented. These classes describe 43% of all easterly regime rainfall and 41% of westerly regime rainfall and, therefore, represent a significant cross section of the data in the selected reflectivity bin. The data have been sorted in order of increasing $\sigma_{Z_{dr}}$ for a cleaner presentation, so there is no significance to the apparent trend with increasing class number in the figure. The dashed and dotted lines present standard deviations over all easterly and westerly pixels, respectively, for reference. Eighty-nine percent of the easterly and 92% of the westerly rain-type classes exhibit reduced $\sigma_{Z_{dr}}$ relative to the regime means. On average, variability in Z_{dr}, which can be thought of as a source of random error in rainfall retrievals, is reduced by ~30% in classifying by rain type.

Similar results are obtained when other reflectivity ranges are examined. Table 2 summarizes the fraction of rainfall in each regime for which the standard deviation of Z_{dr} is reduced through classification. Again, the analysis is restricted to classes with at least 20 samples to ensure robust statistics, but in all cases the resulting subsets provide a representative sample of the full range. Variability in Z_{dr} is reduced for ~90% of the rainfall considered over this wide range of rainfall intensities. Unfortunately, because of the decrease in frequency of observations with higher Z_{sfc}, sufficient statistics could not be compiled for higher reflectivity ranges. Fortunately, however, the data described in Table 2 cover the majority of the reflectivity range for which the easterly and westerly regimes exhibit their greatest Z_{dr} differences (Carey et al. 2001) and, therefore, provide an important test of the classification technique.

While random errors may be reduced through spatial and temporal averaging, biases introduced by systematic changes in DSD, such as those associated with a shift in climate regime, cannot. As a result, it is even more important to assess the degree to which rain-type classification reduces the difference in mean Z_{dr} between the easterly and westerly regimes in LBA. Focusing on the same $36 < Z_{sfc} < 40$ dBZ range, Fig. 8 compares $\overline{Z_{dr}}$ from all rain-type classes mutually observed in both

regimes. Dashed and dotted lines again correspond to the complete easterly and westerly datasets, respectively. Once again to isolate only classes with a statistically significant number of samples, those that occur at least 20 times in both regimes are considered. The 46 classes that make up the resulting subset account for more than 25% of the rainfall in each regime and therefore provide a suitably large sample to be viewed as representative of the properties of the $36 < Z_{sfc} < 40$ dBZ range as a whole. A reduction in the fractional difference in $\overline{Z_{dr}}$ between the regimes is realized in all but 10 of the 46 rain types presented. In terms of the total rainfall at the surface from all pixels in these classes, 78% fall into the rain types with reduced easterly–westerly biases. It is worth noting that the classes for which the Z_{dr} bias is not reduced seem to occur at large $\overline{Z_{dr}}$ suggesting that the microphysical processes leading to the larger raindrops are not captured as well by the vertical and horizontal structure of the reflectivity field. Interestingly, the vertical structures that correspond to these classes are generally more vertically developed than those related to smaller Z_{dr} (as is the case for the dark black profiles shown in Fig. 6 corresponding to the class with the larger Z_{dr} highlighted in Fig. 5d). Perhaps differences in aggregation and riming rates above the freezing level escape detection in the classification process because of the limited sensitivity of the S-Pol to ice particles. This would imply that the raindrop DSD produced by melting the ice particles created by these processes may exhibit systematic differences between the two regimes even if the reflectivity structures are more or less the same below the melting level.

A similar analysis of other reflectivity bins is summarized in Table 3. On average, the bias between the two regimes is reduced for 78% of the total rainfall in each regime. As in Fig. 8, however, there remain a number of classes for which the bias is not reduced in every reflectivity range examined, suggesting that there are factors systematically influencing DSD that are not captured in the reflectivity structure variables chosen for classification, at least not at the resolution adopted here. This is expected because of the complex nature of precipitation development and the fact that none of the classification variables traces the time evolution of the system and, as such, cannot be expected to completely isolate the unique set of microphysical processes within

TABLE 3. As in Table 2, but with respect to reducing Z_{dr} biases between the easterly and westerly regimes. In this case, the fourth and sixth columns present the fraction of the rainfall found in the sample classes for which the bias in Z_{dr} between the regimes is reduced.

Reflectivity range	N	$f_{E,\text{rain}}$	$F_{E,\text{reduced}}$	$f_{W,\text{rain}}$	$F_{W,\text{reduced}}$
28–32	160	52%	76%	54%	76%
32–36	108	47%	64%	56%	69%
36–40	46	29%	83%	26%	76%
40–44	18	34%	95%	27%	90%

it. It is important to note, however, that even in such cases the classification methodology provides a quantitative estimate of the magnitude of the resulting potential bias introduced by the DSD differences that remain within any given class.

Since the properties of many rain-type classes are similar in both the easterly and westerly climate regimes, the disparties in drop size documented by Carey et al. (2001) must be partially attributed to differences in the frequency of occurrence of different rain types in each regime. If this hypothesis is correct, the observed differences in synoptic conditions between the easterly and westerly wind periods in TRMM-LBA and the resulting changes in mean DSDs should manifest themselves in the mean vertical and horizontal structure of the observed reflectivity profiles in each regime. Figure 9 compares mean easterly and westerly reflectivity profiles for all pixels with Z_{sfc} between 36 and 40 dBZ. While their near-surface reflectivities are similar, there are a number of differences in the vertical structure of the associated reflectivity profiles. Rainfall in the easterly regime exhibits larger reflectivities between 2.5 and 5.5 km perhaps because of the existence of a larger concentration of supercooled droplets (Cifelli et al. 2002), a more pronounced peak in reflectivity at 4 km, and less horizontal variability than that in the westerly regime.
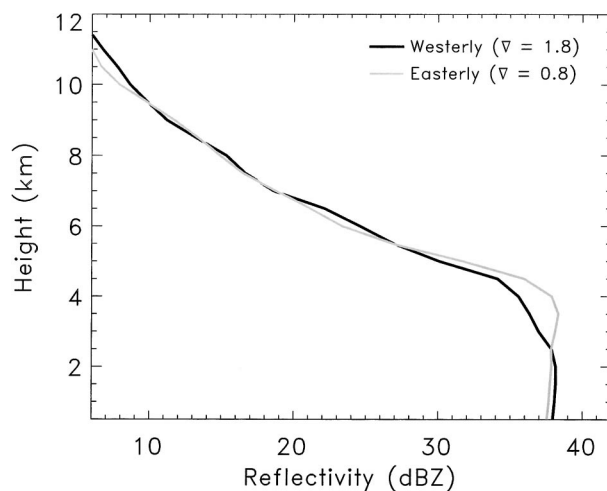

FIG. 9. Mean vertical profiles of reflectivity for all classes with near-surface reflectivity of 38 dBZ (±2) in the easterly (light) and westerly (dark) regimes of LBA.

These findings are consistent with the description of the environmental properties of each regime described in Rickenbach et al. (2002) and Carey et al. (2001). Recall that the lower troposphere is drier in the easterly regime than in the westerly regime, consistent with evaporation at lower levels implied by the reflectivity profiles. Furthermore, the easterly regime has more numerous CCN so a greater fraction of the easterly rainfall likely derives from mixed-phase microphysical processes. This is consistent with the observations of Cifelli et al. (2002), Rickenbach et al. (2002), and Halverson et al. (2002) who report an absence of lighting during westerly rainfall events in TRMM-LBA. These results support the contention that differences in the mechanisms for rainfall formation simultaneously manifest themselves in DSD and in the vertical and horizontal structure of observed reflectivity profiles. Comparison with Fig. 6 suggests that regime-dependent differences in DSD between the easterly and westerly regimes in LBA are partially resolved through the rain-type classification approach described above.

b. CSU-CHILL radar data

Despite the documented differences between the easterly and westerly meteorological regimes in TRMM-LBA, rigorous testing of the uniformity of DSD properties within each rain type requires the examination of precipitation events from a wider variety of synoptic conditions than can be observed in an single location. Data from the CSU-CHILL radar facility in northeastern Colorado are well-suited for this purpose not only because of the similarities between the S-Pol and CHILL radars (for a detailed description of the CSU-CHILL radar facility the reader is directed to http://chill.colostate.edu/CSU-CHILL.html) but, more importantly, because of the contrasting environment for precipitation development they sample. Unlike the widespread precipitation that is encountered during moisture-rich Amazonian wet season, the precipitation that develops in the generally dry eastern Colorado atmosphere generally owes its existence to afternoon thunderstorms that are often accompanied by hail and frequent cloud-to-ground lightning [for a complete description of the different mechanisms governing precipitation formation in the High Plains and subtropics see Cotton and Anthes (1989)]. Thus we anticipate substantial differences in the microphysical processes lead-

TABLE 4. The Z_{dr} properties of classes observed in both the CHILL and LBA datasets. Only pixels with surface reflectivities of 38 ± 2 dBZ are considered.

Class	LBA Sample	LBA mean	σ	CHILL Sample	CHILL mean	σ
All CHILL pixels	0	—	—	2334	1.1711	0.4693
All LBA pixels	17 941	0.8217	0.3558	0	—	—
Class 1	9	0.8223	0.1924	8	0.8828	0.6569
Class 2	25	0.7578	0.3757	6	0.8315	0.2757
Class 3	18	1.0078	0.4985	8	0.8509	0.2495
Class 4	48	0.7480	0.1806	8	0.7271	0.2129
Class 5	18	0.9121	0.2809	8	0.8346	0.2155

ing to precipitation formation in each region and equivalent differences in the resulting DSD and observed reflectivities. Provided the data are stratified into rain types by their three-dimensional reflectivity structures, however, the DSDs in both regions should be similar.

The data employed in the present study consist of 35 scans from four distinct precipitation events observed by the CHILL radar in northeastern Colorado between 2 August 2001 and 24 August 2002. These data were screened for hail in order to avoid contamination in their Z_{dr} signatures that masks its relationship to DSD. These cases span a number of different examples of summertime precipitation, ranging from a large area of widespread precipitation surrounding the radar (approximately 200 km across) with a number of embedded heavier convective elements to an organized line of convection that developed just to the east of the radar and propagated out onto the plains in eastern Colorado. Mean properties of all TRMM-LBA and CHILL pixels with near-surface reflectivities between 36 and 40 dBZ are compared in Table 4 along with properties of the five rain types that are encountered at least five times in both datasets. Note that in this case a mutual class as redefined as only requiring a minimum of 5 occurrances in both the CHILL and LBA datasets as opposed to the 20 occurances required in the comparison of easterly and westerly regimes in LBA. This is necessary

because the rainfall classes overlap much less frequently in these very disparate climates.

The raindrops observed by the CHILL radar are substantially larger than those found during TRMM-LBA for the reflectivity range considered. This is likely a result of enhanced evaporation at lower levels and the predominance of mixed-phase microphysics in Colorado. In addition, it has been speculated that some of the raindrops in High Plains thunderstorms may have stabilizing ice cores, reducing the effects of drop break-up and allowing larger raindrops to survive than would be found in more humid tropical regions (Ryzhkov and Zrnic 1996). Remarkably, the Z_{dr} bias between the datasets (i.e., the difference between the values in the third and sixth columns of Table 2) is reduced by at least a factor of 2 in every one of the five classes mutually found in both datasets. This dramatic improvement is likely due to the more extreme differences in the large-scale environments encountered in each region than those that exist between the easterly and westerly regimes in LBA. The large differences in the corresponding mean vertical profiles of radar reflectivity presented in Fig. 10a confirm that this is the case. Unlike the subtle differences in the reflectivity profiles corresponding to the easterly and westerly regimes during TRMM-LBA (Fig. 9), the CHILL data exhibit a much lower and more pronounced melting level, a substantially larger ice con-
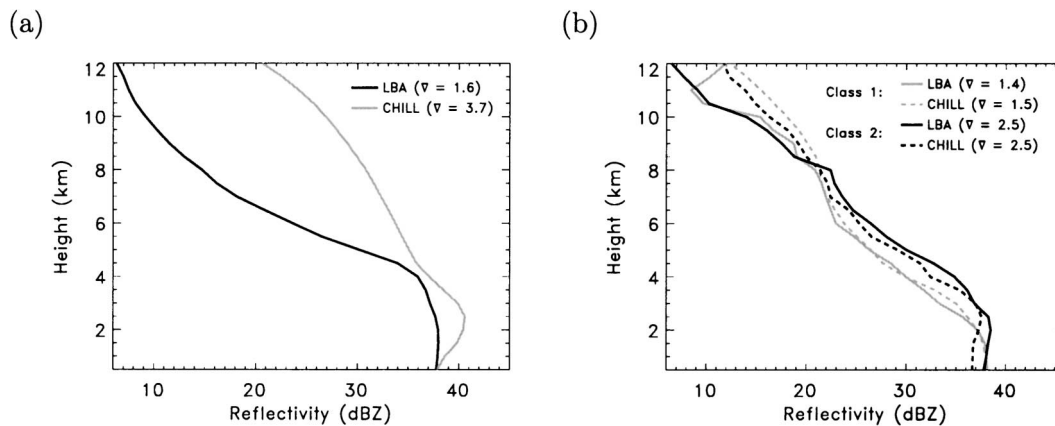

FIG. 10. Mean reflectivity profiles for (a) all classes with near-surface reflectivity of 38 dBZ (± 2) from the CHILL (light) and LBA (dark) datasets, and (b) classes 1 and 2 from Table 2 observed in both CHILL and LBA. In each case, mean horizontal gradients between nearest neighbors are provided in parentheses in the legend.

tent aloft, significantly greater evaporation at lower levels, and more horizontal inhomogeneity than their counterparts from TRMM-LBA. When the analysis is restricted to pixels with similar profiles (which presumably share more common microphysical processes), such as those presented in Fig. 10b, the biases in the raindrop DSD one would infer from the corresponding Z_{dr} measurements is substantially reduced. These results support the hypothesis that it may be possible to exploit the connection between microphysics, DSD, and three-dimensional reflectivity structure to reduce random and systematic errors in the DSD assumptions employed in single-parameter radar rainfall retrieval algorithms. Even though the environment and mechanisms surrounding precipitation formation in Colorado and in the Amazon are very different, the DSDs for pixels found in both regions that share the same vertical and horizontal reflectivity structures are generally similar.

4. Rain types on global scales

a. Exporting LBA-defined rain types elsewhere in the Tropics

These results suggest that objectively classifying pixels according to the vertical and horizontal structure of their observed reflectivity fields provides an additional constraint on rainfall retrievals, but only observations that can be directly assigned to rain types observed in the presence of explicit DSD measurements (e.g., from polarimetric radars, disdrometers, or profilers) will benefit from the classification approach. It is therefore important to determine the degree to which the rain types observed in TRMM-LBA are representative of rainfall elsewhere in the Tropics. To this end, TRMM PR data from the months of December 1999, January 2000, and February 2000 have been classified according to Table 1 to determine the fraction of rainfall that actually falls into classes observed in the TRMM-LBA field campaign. Figure 11 presents the fraction of rainfall that can be attributed to rain-type classes defined in TRMM-LBA for all $5° \times 5°$ grid boxes in the Tropics. On average, 22% of the rainfall observed by TRMM falls into reflectivity-based rain-type categories observed in LBA. Some regions, however, are much better represented by LBA than others. Conventional wisdom would suggest that one should look to a land-based site to study continental precipitation and an ocean-based site to examine oceanic precipitation. Figure 11, on the other hand, suggests that the rainfall observed in LBA is more representative of that occurring the west Pacific (where almost 40% of the local rain falls into classes observed in LBA) than the rain systems found in South Africa. It is worth nothing that Rondonia, Brazil, has been termed the "Green Ocean" by several researchers (e.g., Williams et al. 2002), consistent with this finding.

To accurately assign a DSD and an associated uncertainty to a rain-type category it must, of course, be observed often enough that sufficient statistics can be accumulated to define its properties. The lowest panel of Fig. 11 restricts the comparison to classes that are observed a minimum of 20 times in LBA. In general, the structure of the map mimics that in the middle panel, but the fraction of rainfall that falls into rain types observed in LBA is substantially reduced. Overall, the LBA rain types for which appropriate statistics exist characterize 3.6% of all rainfall observed by TRMM. Furthermore, the fact that 6 times as much rainfall falls into classes with fewer than 20 samples suggests that a longer field campaign in the same region should allow us to accumulate sufficient statistics to define the properties of a much greater fraction of tropical rainfall. Noting that the LBA S-Pol data cover only 50 days over a region that represents less than one ten-thousandth (0.0098%) of the TRMM sampling area,[3] these results are promising.

b. Toward a new strategy for validating global rainfall products

As stated at the outset, satellite-derived climate records are susceptible to regime-dependent systematic errors in algorithm parameters that are not explicitly measured by the satellite. Assessing the magnitude of the biases introduced by such errors requires extending modern algorithm validation beyond the classical approach of evaluating retrieved products to verify the assumptions used to obtain them. In light of the results presented here, a new philosophy for algorithm validation emerges. All unobserved assumptions in the algorithm are treated as soft constraints and weighted according to how well they can be prescribed by auxiliary external validation. In this framework, the retrieval process can be thought of as an error propagator that uses the uncertainties in both the measurements and assumed parameters in conjunction with a physical model to infer a set of desired retrieval products with associated uncertainties. This approach places equal importance on assessing the uncertainties in assumed parameters as it does on making the observations themselves. In the context of the rainfall retrieval problem, therefore, it is equally valuable to assess the means and standard deviations of the polarimetric observations assigned to any given rain-type class as it is to verify the retrieved rainfall rate.

Adopting this philosophy has implications for future precipitation missions, such as the Global Precipitation Measurement (GPM) mission. If such an approach is adopted, it will be necessary for validation programs connected to these missions to focus on obtaining collocated ground-based measurements of DSD and three-dimensional maps of radar reflectivity from a broad range of precipitation systems to improve confidence in

---

[3] The area sampled by the S-Pol is $\sim 3.1 \times 10^4$ km², while the area of sampled by TRMM ($\pm 40°$ latitude) is $\sim 3.2 \times 10^8$ km².
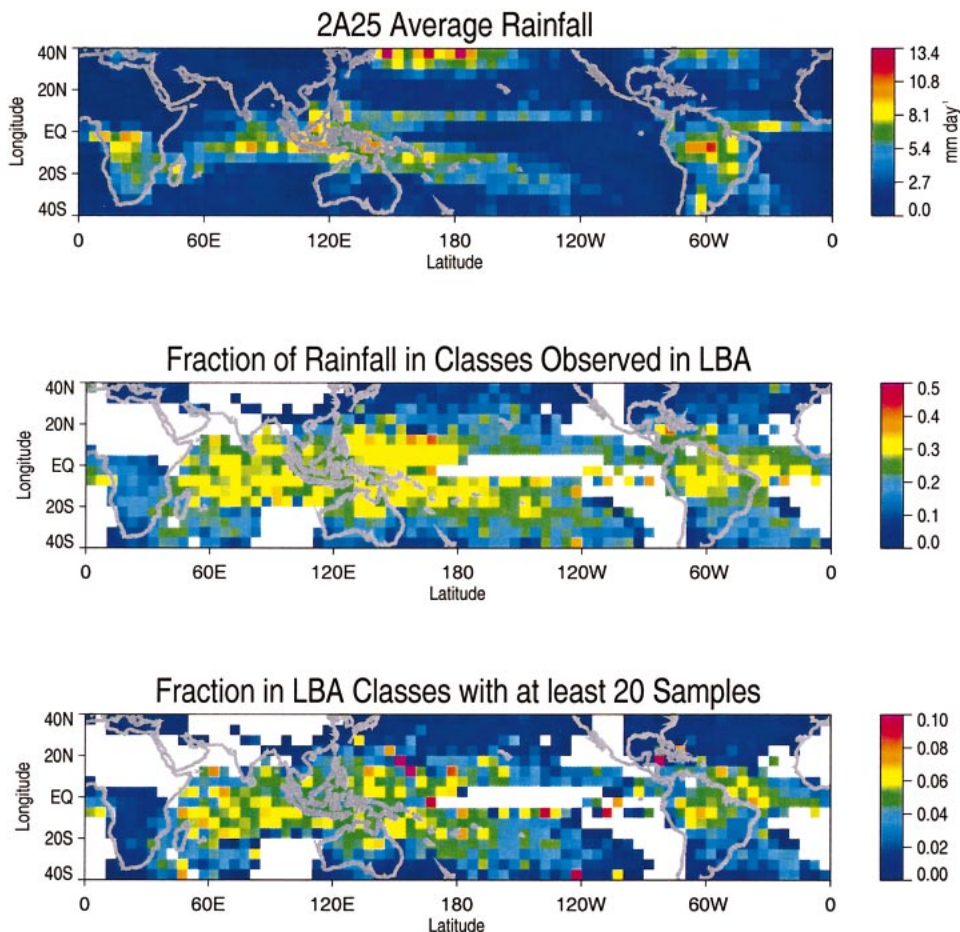
FIG. 11. Mean rainfall at $5° \times 5°$ resolution from the PR-based 2A25 product for (top) the months of Dec 1999 through Feb 2000, (middle) the fraction of this rainfall that falls into classes observed in the TRMM-LBA experiment, and (bottom) the fraction that falls into LBA-defined classes with at least 20 samples.

the results and represent a higher fraction of global rainfall. Furthermore, through maps such as those produced in the preceding section, the method itself provides a means for assessing where validation sites need to be placed. Careful analysis of regions where a significant fraction of precipitation falls in rain types not characterized by existing validation data may provide insight into the best sites to conduct future experiments. Given a choice of proposed future validation sites, for example, global maps of the spatial correlations between the rain types observed by the satellite at each site and those observed elsewhere should indicate the site or sites that have the greatest potential for filling in information about missing classes.

Two such maps are presented in the middle and lower panels of Fig. 12 that investigate the representativeness of rainfall in the northern South Africa and Cape Hatteras, North Carolina, regions, respectively. Comparing with Fig. 11, it is apparent that ground-based polarimetric radar observations in South Africa would provide substantial information to complement those made in

the Amazon. As one would expect, the rain types defined in this region clearly describe those found elsewhere in the African continent but, less expectedly, they also appear to be representative of those found in subtropical oceanic regions, an area poorly characterized by the TRMM-LBA rain types. Similar observations taken off the east coast of North Carolina, on the other hand, may represent some of the precipitation occurring in the winter hemisphere subtropics but contain little or no rain types observed elsewhere in the Tropics. As a result, it is perhaps a less attractive site for future field experiments if they are directed at validating tropical rainfall estimates. To fully assess the benefits of any given site it is important to consider a much longer time period than the 3 months analyzed here, and the expected duration of the field experiment must be accounted for. Polarimetric radar sites that operate on a more continuous basis, like the CSU-CHILL radar facility, for example, provide invaluable sources of data, as they complement intensive observation periods in field campaigns with continuous observations over a longer time
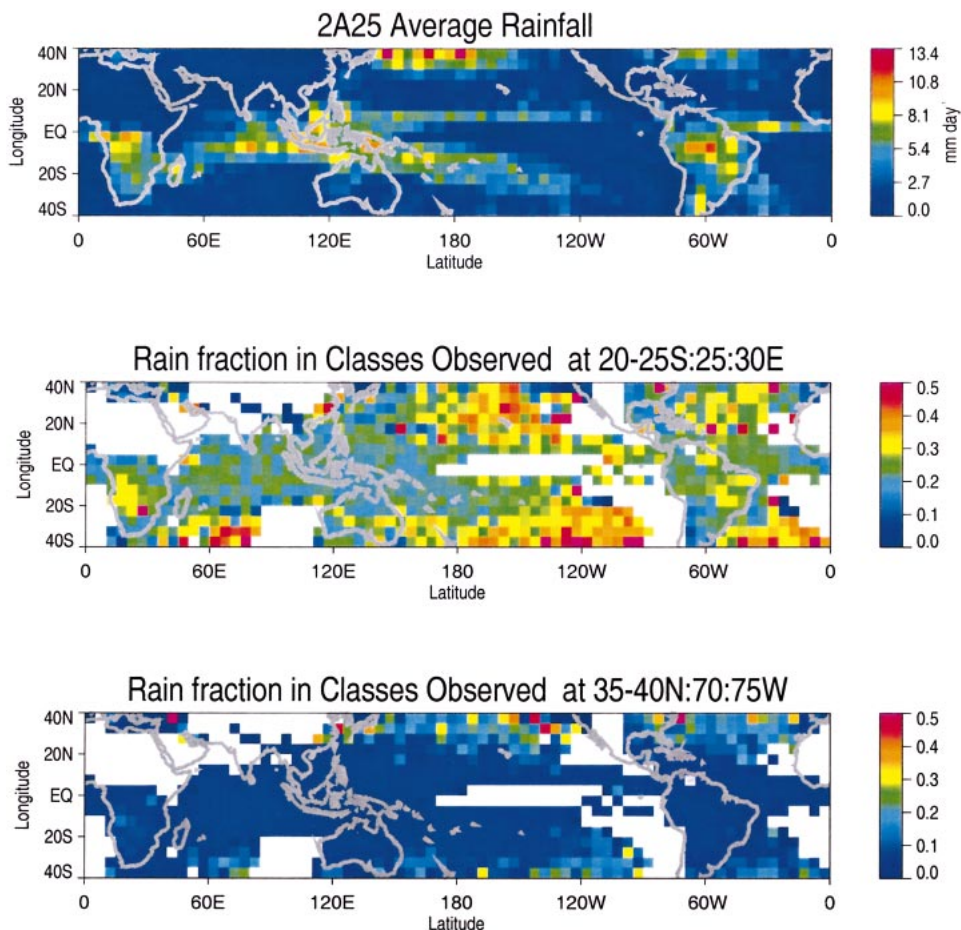
FIG. 12. As in Fig. 11 except that the lower two panels represent the fraction of rainfall that falls into classes observed in 5° × 5° boxes located in (middle) northern South Africa (20°–25°S, 25°–30°E) and (bottom) Cape Hatteras, NC, (35°–40°N, 70°–75°W) regions, respectively.

frame from which a diverse collection of precipitation events can be accumulated.

5. Discussion

The preceding analyses, while preliminary in nature, suggest that classifying rainfall by the three-dimensional structure of its reflectivity field offers the potential to reduce both random and systematic errors in DSDs assumed in global rainfall retrievals. Furthermore, differences in the polarimetric observations corresponding to identical rain types observed in different field campaigns provide an estimate of possible regime-dependent systematic errors that results from the fact that rain types can never be perfectly defined. Random variability within the rain types themselves, on the other hand, provides an estimate of random errors in model assumptions that can be propagated through the retrieval via an end-to-end error model to estimate retrieval uncertainties. Within this framework the key to algorithm validation shifts from direct verification of products susceptible to climate-regime-dependent biases that cannot

be removed from the data, to determining the uncertainties in the principal assumptions required to constrain the algorithm. Subsequently, through the identification of similar rain types occurring around the world, rain-type classification provides a means for exporting the information learned in these comprehensive ground validation experiments to quantify satellite uncertainties on a global scale. In addition, as more data become available and our confidence in the properties of rain-type classes increases, the results can be used to supply crude estimates of Z_{dr} and K_{dp} to radars with no polarization capability. In this way, biases in rainfall products arising from climate regime dependences can be partially mitigated.

The fact that some DSD differences often remain even after classification implies that other factors influence DSD beyond those considered here. Further study will be required to assess the role played by aerosol type and concentration, wind shear, buoyancy, and other factors in determining DSD and to further delineate dynamical and microphysical environmental regimes for precipitation formation. Such an analysis will also be

necessary to reconnect the reflectivity-based classification scheme outlined here to the ground-based approaches centered on identifying climate regimes. Additional field campaigns and longer duration experiments are also needed to both characterize rain-type classes that were not observed in LBA and accumulate better statistics to improve our level of confidence in those that were. Furthermore, it will be necessary to supplement polarimetric radar observations with other measures of DSD such as those provided by disdrometers and wind profilers in order to verify the findings and quantify the degree to which the DSD itself is constrained through classification. Even so, the method presented here provides a means for amalgamating ground-based observations into a seamless framework for algorithm development and validation in the future. In principle, the philosophy of objectively classifying data and validating uncertainties can be adapted to the complete set of assumptions required in any physically based retrieval algorithm provided care is taken to frame the problem in terms of a suitable set of observables.

REFERENCES

Amitai, E., 2000: Systematic variation of observed radar reflectivity–rainfall rate relations in the Tropics. *J. Appl. Meteor.,* **39,** 2198–2208.

Battaglia, A., C. Kummerow, D.-B. Shin, and C. Williams, 2003: Constraining microwave brightness temperatures by radar brightband observations. *J. Atmos. Oceanic Technol.,* **20,** 856–871.

Battan, L. J., 1973: *Radar Observations of the Atmosphere.* University of Chicago Press, 324 pp.

Beard, K. V., and C. Chuang, 1987: A new model for the equilibrium shape of raindrops. *J. Atmos. Sci.,* **44,** 1509–1524.

Berg, W., C. Kummerow, and C. A. Morales, 2002: Differences between east and west Pacific rainfall systems. *J. Climate,* **15,** 3659–3672.

Boccippio, D. J., 2003: Archetypal TRMM radar profiles identified through cluster analysis. Preprints, *31st Conf. on Radar Meteorology,* Seattle, WA, Amer. Meteor. Soc., 510–513.

Bringi, V. N., and V. Chandrasekar, 2001: *Polarimetric Doppler Weather Radar: Principles and Applications.* Cambridge University Press, 636 pp.

Carey, L. D., R. Cifelli, W. A. Peterson, and S. A. Rutledge, 2000: Preliminary report on TRMM-LBA rainfall estimates using the S-POL radar. Paper 697, Department of Atmospheric Science, Colorado State University, 19 pp.

——, ——, ——, ——, and M. A. F. Silva Dias, 2001: Characteristics of Amazonian rain measured during TRMM-LBA. Preprints, *30th Int. Conf. on Radar Meteorology,* Munich, Germany, Amer. Meteor. Soc., 682–684.

Cifelli, R., W. A. Petersen, L. D. Carey, and S. A. Rutledge, 2002: Radar observations of the kinematic, microphysical, and precipitation characteristics of two MCSs in TRMM LBA. *J. Geophys. Res.,* **107,** 8077, doi:10.1029/2000JD000264.

Cotton, W. R., and R. A. Anthes, 1989: *Storm and Cloud Dynamics.* Academic Press, 883 pp.

Halverson, J. B., T. Rickenbach, B. Roy, H. Pierce, and E. Williams, 2002: Environmental characteristics of convective systems during TRMM-LBA. *Mon. Wea. Rev.,* **130,** 1493–1509.

Huffman, G. J., and Coauthors, 1997: The Global Precipitation Climatology Project (GPCP) combined precipitation dataset. *Bull. Amer. Meteor. Soc.,* **78,** 5–20.

Iguchi, T., T. Kozu, R. Meneghini, J. Awaka, and K. Okamoto, 2000: Rain-profiling algorithm for the TRMM Precipitation Radar. *J. Appl. Meteor.,* **39,** 2038–2052.

Jameson, A. R., 1983: Microphysical interpretation of multi-parameter radar measurements in rain. Part I: Interpretation of polarization measurements and estimation of raindrop shapes. *J. Atmos. Sci.,* **40,** 1792–1802.

Joss, J., and A. Waldvogel, 1967: A raindrop spectrograph with automatic analysis. *Pure Appl. Geophys.,* **68,** 240–246.

Kummerow, C. D., P. Poyner, W. Berg, and J. Thomas-Staehle, 2004: The effects of rainfall inhomogeneity on climate variability of rainfall estimated from passive microwave sensors. *J. Atmos. Oceanic Technol.,* **21,** 624–638.

Lee, G. W., 1990: Errors in rain measurement by radar: Effect of variability of drop size distributions. Ph.D. thesis, McGill University, 279 pp.

McCarthy, J. J., O. F. Canziani, N. A. Leary, D. J. Dokken, and K. S. White, Eds., 2001: *Climate Change 2001: Impacts, Adaptation and Vulnerability.* Cambridge University Press, 1000 pp.

Nesbitt, S. W., E. J. Zipser, and D. J. Cecil, 2000: A census of precipitation features in the Tropics using TRMM: Radar, ice scattering, and lightening observations. *J. Climate,* **13,** 4087–4106.

Petersen, W. A., S. W. Nesbitt, R. J. Blakeslee, R. Cifelli, P. Hein, and S. A. Rutledge, 2002: TRMM observations of intraseasonal variability in convective regimes over the Amazon. *J. Climate,* **15,** 1278–1294.

Poyner, P., 2002: Beam-filling correction variability in emission-based passiver microwave rainfall retrievals. M.S. thesis, Colorado State University, 99 pp.

Rickenbach, T. M., R. N. Ferreira, J. Halverson, D. L. Herdies, and M. A. F. Silva Dias, 2002: Modulation of convection in the southwestern Amazon basin by extratropical stationary fronts. *J. Geophys. Res.,* **107,** 8040, doi:10.1029/2000JD000263.

Robertson, F. R., D. E. Fitzjarrald, and C. D. Kummerow, 2003: Effects of uncertainty in TRMM precipitation radar path integrated attenuation on interannual variations of tropical oceanic rainfall. *Geophys. Res. Lett.,* **30,** 1180, doi:10.1029/2002GL016416.

Rosenfeld, D., E. Amitai, and D. B. Wolff, 1995: Classification of rain regimes by the three-dimensional properties of reflectivity fields. *J. Appl. Meteor.,* **34,** 198–211.

Ryzhkov, A. V., and D. S. Zrnic, 1996: Rain in shallow and deep convection measured with a polarimetric radar. *J. Atmos. Sci,* **53,** 2989–2996.

Sempere-Torres, D., R. Sanches-Diezma, I. Zawadzki, and J. D. Creutin, 1999: DSD identification following a pre-classification of rain-type from radar analysis. Preprints, *29th Conf. on Radar*

Meteorology, Montreal, QC, Canada, Amer. Meteor. Soc., 632–635.

——, ——, ——, and ——, 2000: Identification of stratiform and convective areas using radar data with application to the improvement of DSD analysis and *Z–R* relations. *Phys. Chem. Earth,* **25,** 985–990.

Steiner, M., R. A. Houze Jr., and S. E. Yuter, 1995: Climatological characterization of three-dimensional storm structure from operational radar and rain guage data. *J. Appl. Meteor.,* **34,** 1978–2007.

Uijlenhoet, R., M. Steiner, and J. A. Smith, 2003: Variability of raindrop size distributions in a squall line and implications for radar rainfall estimation. *J. Hydrometeor.,* **4,** 43–61.

Williams, E., and Coauthors, 2002: Contrasting convective regimes over the Amazon: Implications for cloud electrification. *J. Geophys. Res.,* **107,** 8082, doi:10.1029/2001JD000380.

Xie, P., and P. A. Arkin, 1996: Analyses of global monthly precipitation using guage observations, satellite estimates, and numerical model predictions. *J. Climate,* **9,** 840–858.

——, and ——, 1997: Global precipitation: A 17-year monthly analysis based on guage observations, satellite estimates, and numerical model outputs. *Bull. Amer. Meteor. Soc.,* **78,** 2539–2558.

Zawadzki, I., and A. Bellon, 2003: Error statistics of VPR corrections in stratiform precipitation. Preprints, *31st Conf. on Radar Meteorology,* Seattle, WA, Amer. Meteor. Soc., 225–228.

Zhang, G., J. Vivekanadan, and E. Brandes, 2001: A method for estimating rain rate and drop size distribution from polarimetric radar measurements. *IEEE Trans. Geosci. Remote Sens.,* **39,** 830–841.